Supplementary Information

Plasma lattice-matched interfacial engineering enables boosted photocatalytic O_2 activation for antibiotic degradation

*Junjie Chen[a,#], Zihan Fu[a,#], Zhimin Dong[a, *], Zhiqing Lin[b], Yaoxuan Wang[a], Zifan Li[a], Youqun Wang[a], Zhibin Zhang[a, *], Bin Han[b, *] and Yunhai Liu[a, c]*

[a] National Key Laboratory of Prospecting, Mining and Remote Sense Detecting on Uranium Resources, East China University of Technology, Nanchang 330013, P.R. China

[b] Guangdong Basic Research Center of Excellence for Ecological Security and Green Development, Guangdong Provincial Key Laboratory of Water Quality Improvement and Ecological Restoration for Watersheds, School of Ecology, Environment and Resources, Guangdong University of Technology, Guangzhou 510006, P.R. China

[c] Gandong University, Fuzhou 344000, China

[*]Corresponding author: *Prof.* Zhimin Dong, E-mail: 202163003@ecut.edu.cn

Prof. Zhibin Zhang, E-mail: zhbzhang@ecut.edu.cn

Prof. Bin Han, E-mail: hanbin@gdut.edu.cn

[#]These authors contributed equally to this work.

Experimental Procedures

S1 Chemistry Reagents

Thiourea (CH_4N_2S, 99.5%), potassium bromide ($BiBr_3$, 99.9%), and anhydrous ethanol (C_2H_5OH, AR) were purchased from Shanghai Titan Scientific Company, Ltd. All reagents were branded as Adamas-beta, Adamas-life. All of the chemicals were of analytical grade and were utilized in the tests without any additional processing. The study was conducted using deionized water.

S2 Characterization

The distribution, size, and morphology of the as-prepared samples were characterized by TEM and HRTEM (JEOL, Japan). The elemental mapping of the materials was performed by element mapping. The crystal structure of the products was characterized by X-ray diffraction (XRD, Bruker D8 Advance diffractometer) within 2θ range from 5° to 80° with Cu Kα radiation (λ = 0.15418 nm) at a scan rate of $0.05°\cdot s^{-1}$. The structure of the compound was further confirmed by Fourier-transform infrared spectroscopy (Nicolet 6700, Thermo, USA) at the wavelength of 4000-500 cm^{-1}. The valence state and surface energy state distribution of photocatalysts were obtained using XPS (Escalab 250Xi, Thermo Fisher Scientific, USA). The UV-Vis Diffuse Reflectance Spectroscopy (UV-Vis DRS) was tested on a Hitachi U-300 with a scanning range of 200-1500 nm and a white standard of $BaSO_4$ was used as a reference. Electron paramagnetic resonance (EPR) was obtained on an ESR spectrometer (MEX-nano, Bruker) with a modulation frequency of 100 kHz and a microwave power of 15 mW. The energy band gap (Eg) of the as-synthesized photocatalysts was calculated according to the UV-vis absorption spectra. The surface potential values were recorded in lift mode with a lift height of 100 nm, with a resolution of 256 samples/line and a scan rate of 0.4 Hz. Electrochemical tests such as electrochemical impedance (EIS), transient photocurrent (TPCR) and Mott-Schottky (M-S) curves were measured in a conventional three-electrode configuration by an electrochemical analyzer CHI 660D electrochemical workstation (Chen Hua, Shanghai, China). The electrochemical

Rotating Disk Electrode (RDE) measurements were conducted using a CHI760e electrochemical workstation in a three-electrode configuration cell. PL spectra were recorded on an Edinburgh FS5 spectrofluorometer in the range of 390 - 800 nm. The Zeta potential of PFBTD was assessed on a zeta sizer (ZS90, Malvern Zeta sizer Nano, UK). Dark adsorption was continued for 60 min before illumination. Photo-irradiated Kelvin probe force microscopy (KPFM) was performed on SPM-9700 (Shimadzu, Japan).

S3 Photodegradation performance evaluation and application

For recycling tests, the photocatalyst were washed with distilled water and dried in an oven at 60°C. The dried catalysts were reused for the next run for OFX degradation. For the free radical trapping experiment, 3 mmol·L^{-1} potassium bromate ($KBrO_3$), methanol (MeOH), tert-butanol (TBA) and p-benzoquinone (p-BQ) were selected as scavengers for e^-, h^+, $\cdot O_2^-$ and ·OH, respectively. Specifically, the photocatalyst (10 mg) was dispersed in 50 mL of OFX (10 mg·L^{-1}) aqueous solution. The above solution was irradiated for a certain time, then collected and filtered with 0.22 μm PES membrane to remove photocatalyst. NBT detection $\cdot O_2^-$: 20 mg sample and 50 mL NBT solution (0.1mmoL·L^{-1}) were mixed and dispersed in a jacketed Shi Ying beaker. The jacketed Shi Ying beaker was irradiated by a 300W xenon lamp (with cut-off filter > 420nm) and cooled by circulating water. After irradiation at different times, 2.0m suspension was sucked with a straw, then filtered with a 0.22um filter membrane, and the ultraviolet-visible spectrum was collected. Coumarin fluorescence detection ·OH: 10 mg of material is dispersed in 50 mL of coumarin solution (1mmol·L^{-1}), 2mL of suspension is taken at intervals of 5 min to filter out the supernatant, and the fluorescence spectrum is detected at the excitation wavelength of 390nm (the luminescence signal is at 460 nm) by fluorescence spectrometer. The stronger the fluorescence signal, the more ·OH is generated. Quantitative determination of H_2O_2: After photocatalysis, mix 1m supernatant solution with 1mL potassium titanium oxalate solution (0.1mol·L^{-1}) and let it stand in the dark for 60min. At the wavelength of 385nm, the absorbance of the

mixed solution was measured by an ultraviolet-visible spectrophotometer, and then the H_2O_2 concentration ($\mu mol \cdot L^{-1}$) was calculated by the converted formula.

S4 Theory and calculation

We simulated the process of plasma etching BBS nanorods at different time by Monte Carlo. Begin with a reactive ion etching (RIE) model where surface morphology evolution follows the equation :[S1]

$$\frac{\partial h}{\partial t} = v^2 h - k\nabla^4 h - \sqrt{1 + (\nabla h)^2}[S_0F_0 + S_1F_1 + \ldots] + \eta \qquad \text{Equation S1}$$

Here S_n represents the etching probability for n-times reflected particles, and F_n denotes the flux of nth-order particles. Under typical plasma etching conditions (pressure ~10^{-3} Pa, temperature ~10^2 K), particles obey classical statistical distributions. The mean free path significantly exceeds the particle-surface distance, enabling collision-free particle trajectories. This justifies treating particles independently and assuming surface morphology stabilization over time. F_o equals $\sqrt{1 + (\nabla h)^2}$ for normal incidence without shadowing effects, while oblique incidence requires shadowing corrections. Our modified sputter etching model implements simplified physical assumptions through these rules:(1) The etching surface is discretized into an L×L matrix where matrix values represent local heights (initialized at Z). Each etching event decreases the value by 1 unit; (2) Etchant particles are introduced at random (x,y) positions above the surface (Z+1 height). Particles are categorized by energy: high-energy particles strike vertically, while low-energy ones approach with random angles. High-energy particles always etch upon contact then rebound, whereas low-energy particles may either etch or rebound; (3) Single-particle tracking with straight trajectories and periodic boundary conditions is implemented, neglecting plasma diffusion effects; (4) Only first-reflection events are considered, with rebounded particles either re-impacting ($S_1 = 1$) or escaping.

This particle-driven approach, governed by three key parameters - particle count (n), energy threshold (E), and rebound probability (S_o) - fundamentally differs from

conventional RIE models by emphasizing directional sputtering effects over collective plasma interactions. The simplified framework enables efficient simulation of surface evolution dominated by ballistic particle-surface interactions and geometric shadowing effects.

The intermediates from OFX photodegradation by BBS/BOB-2 was identified by combining liquid chromatography (Ultimate 3000 UHPLC-Q Exactive, Thermo Scientific) with a mass spectrometer (Thermo Scientific Q Exactive) (LC-MS). The liquid chromatography was equipped with C18 column (Eclipse Plus) and worked at 308 K. Elution consisted of 0.1 vol% formic acid and acetonitrile at a flow rate (0.3 mL/min). Mass spectra with 50-600 m/z worked in a positive mode using a HESI source. The risk of resulting intermediates was evaluated based on QSAR theory by using the Toxicity Estimation Software Tool (T.E.S.T.5.1.1).

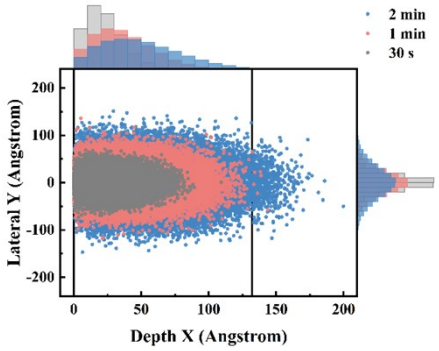

Figure S1. Model the spatial distribution of oxygen diffusion over time when introducing oxygen plasma at a specific injection point within the material.

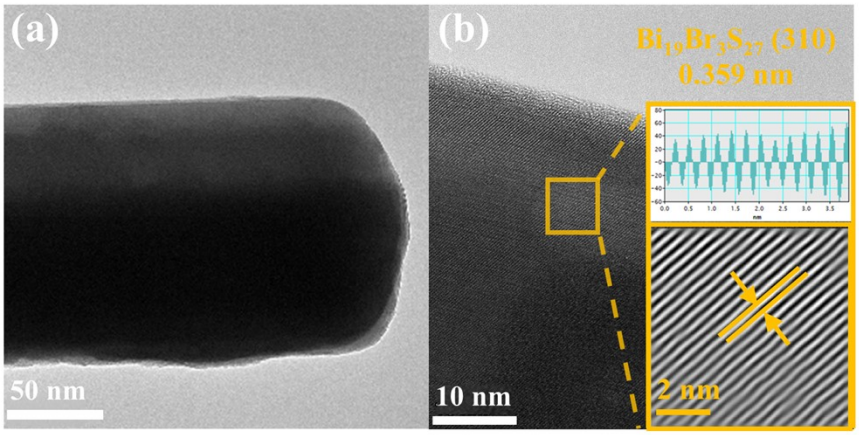

Figure S2. (a) TEM images and (b)HRTEM images, fast inverse Fourier transform and lattice spacing contour map of BBS.

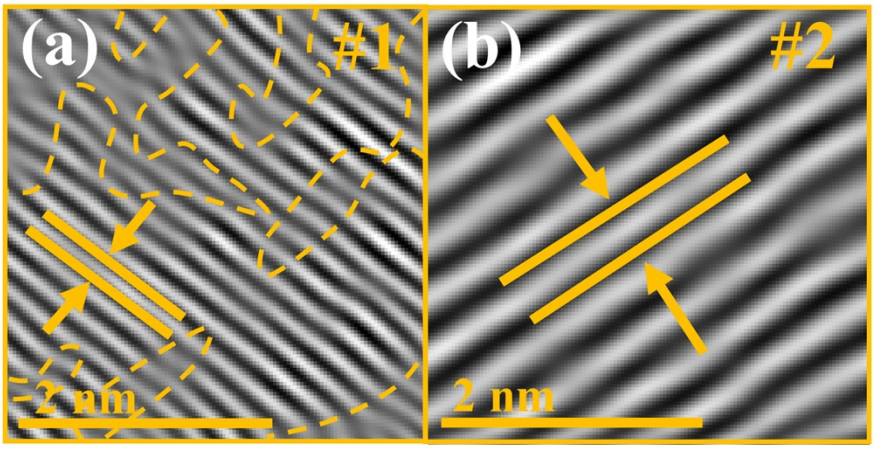

Figure S3. (a,b) fast inverse Fourier transform (IFFT) of BBS/BOB-2 composite.

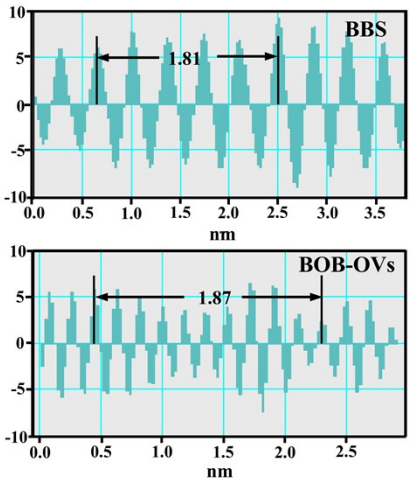

Figure S4. The lattice spacing contour map of BBS/BOB-2 composite.

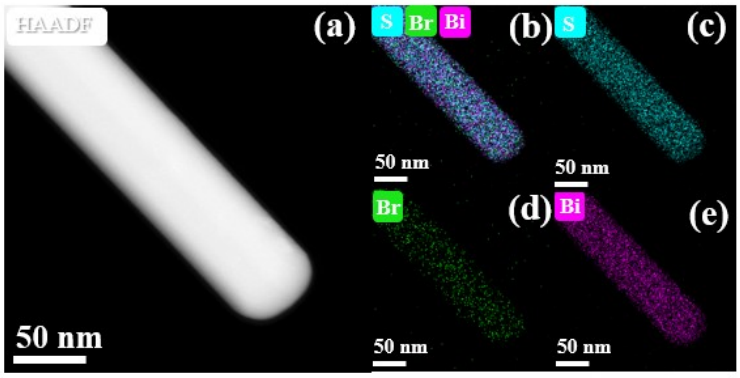

Figure S5. (a) HAADF-STEM image (b-e) elemental mapping images of BBS.

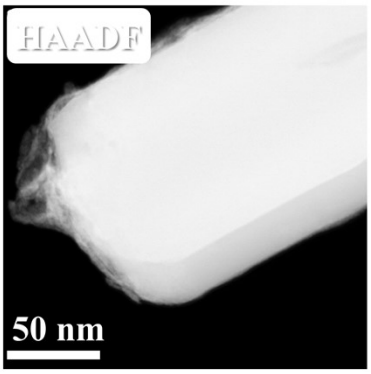

Figure S6. HAADF-STEM image of BBS/BOB-2.

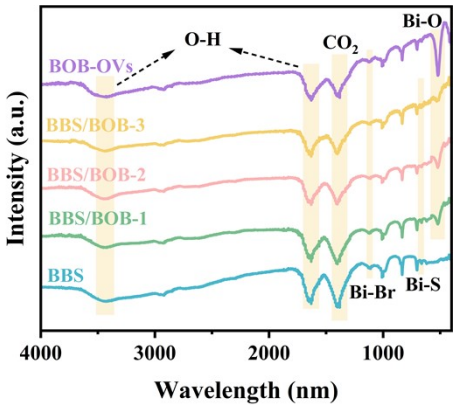

Figure S7. FT-IR spectrum of all samples.

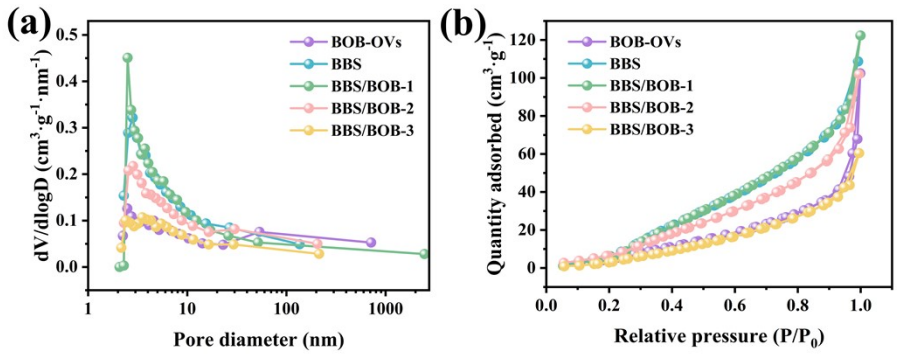

Figure S8. (a) N_2 adsorption-desorption isotherms and (b) pore size distribution of all samples.

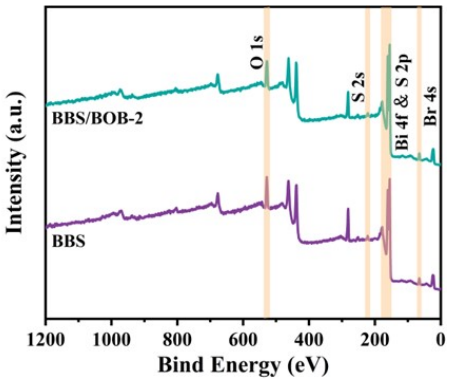

Figure S9. XPS spectra of BBS and BBS/BOB-2.

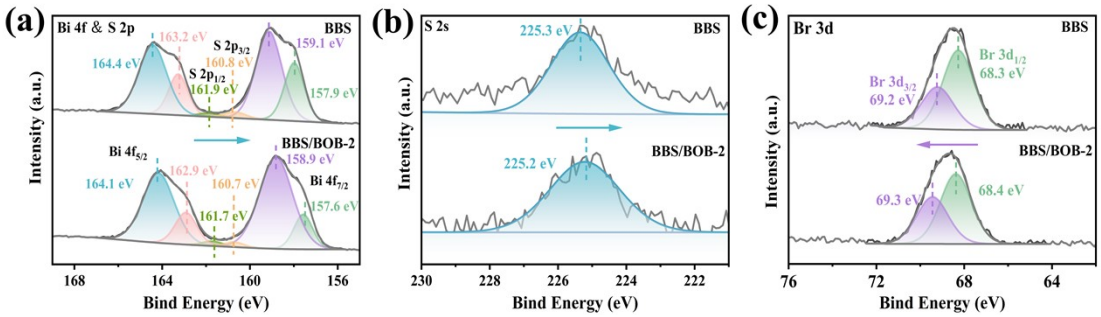

Figure S10. High-resolution XPS spectra of (a) Bi 4f and S 2p, (b) S 2s, and (c) Br 3d, of BBS and BBS/BOB-2.

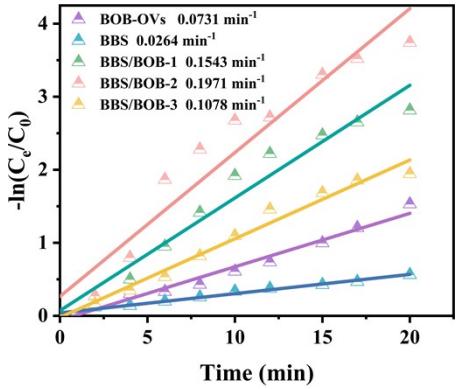

Figure S11. The pseudo-first-order kinetics of OFX solution using BOB-OVs, BBS and BBS/BOB photocatalysts.

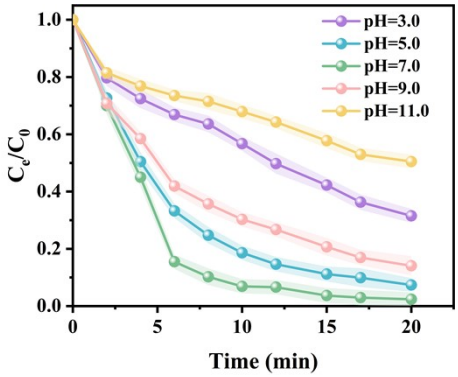

Figure S12. Effects of different pH on degradation rate of OFX.

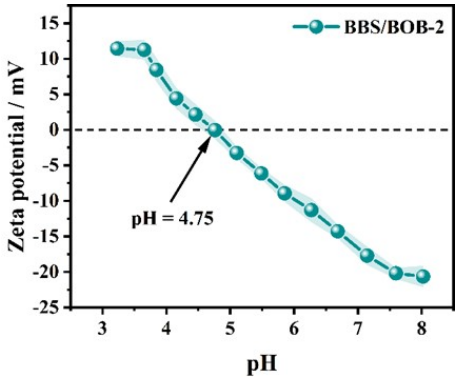

Figure S13. Zeta potential of BBS/BOB-2 photocatalyst.

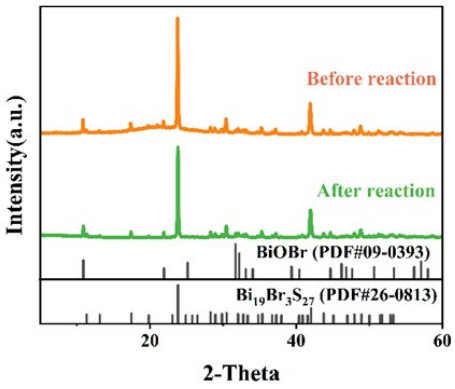

Figure S14. The XRD patterns before and after photocatalytic OFX by BBS/BOB-2.

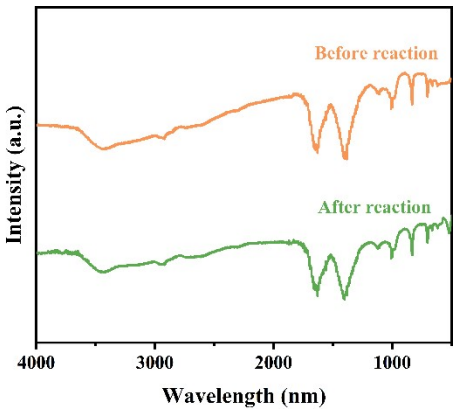

Figure S15. The FT-IR spectrum before and after photocatalytic OFX by BBS/BOB-2.

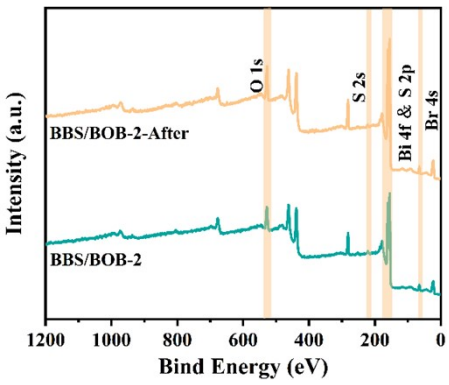

Figure S16. The XPS spectra before and after photocatalytic OFX by BBS/BOB-2.

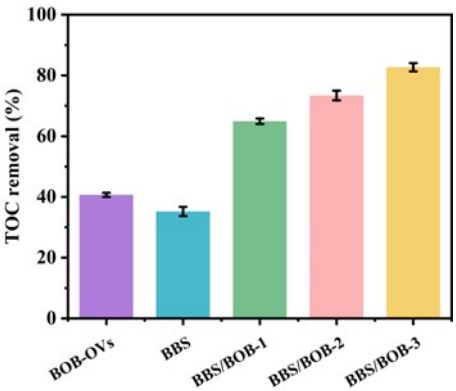

Figure S17. TOC removal of BBS and BBS/BOB-2 system

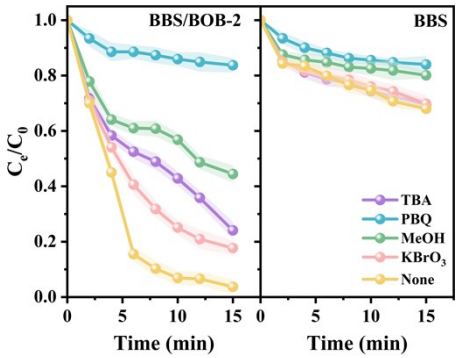

Figure S18. Effects of different quenchers on BBS and BBS/BOB-2 system

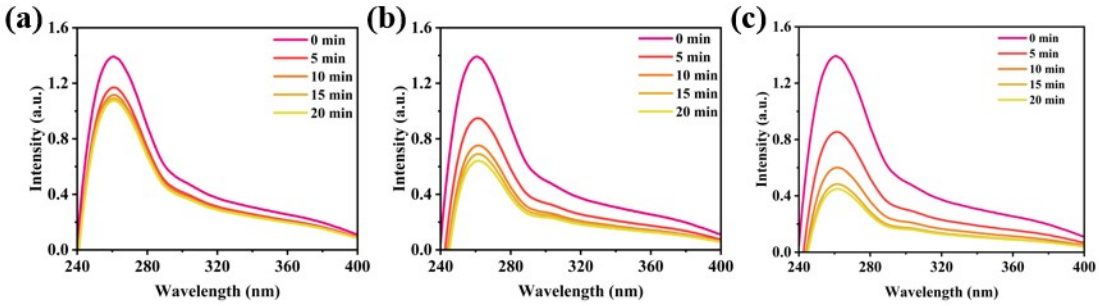

Figure S19. Coumarin test of BBS, BOB-Ovs and BBS/BOB-2.

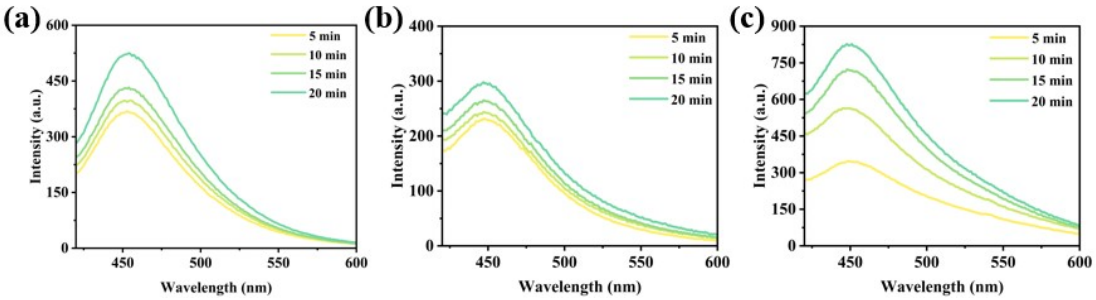

Figure S20. NBT test of BBS, BOB-Ovs and BBS/BOB-2.

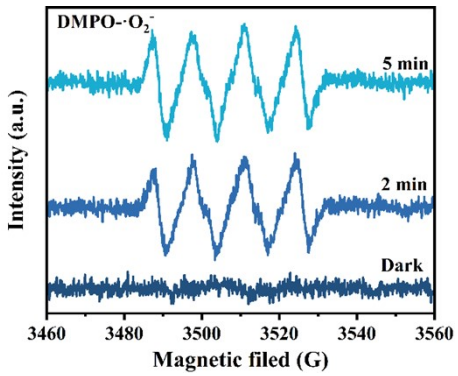

Figure S21. ESR spectra of DMPO - ·O_2^- of BBS/BOB-2.

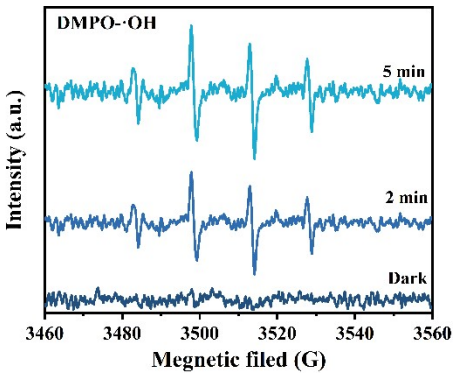

Figure S22. ESR spectra of DMPO - ·OH of BBS/BOB-2.

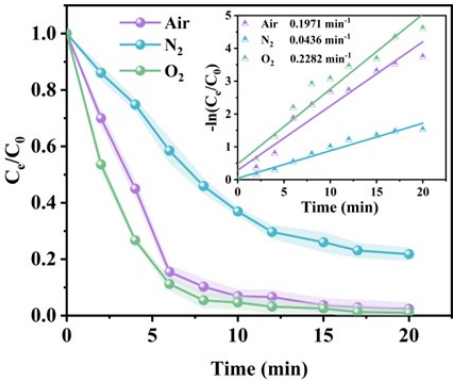

Figure S23. OFX degradation curves with bubbling different gas.

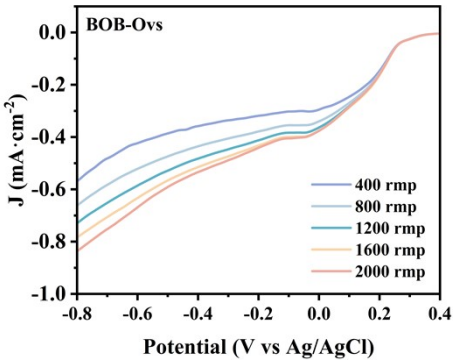

Figure S24. Linear-sweep voltammograms of BOB-Ovs measured on a rotating disk electrode at different rotation speeds.

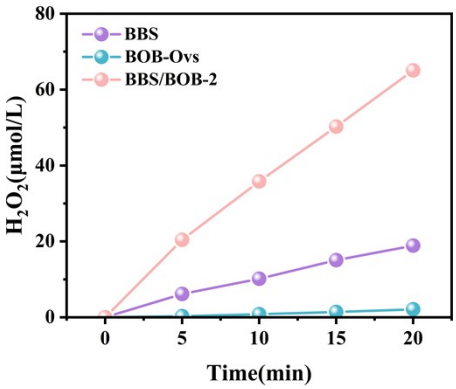

Figure S25. H_2O_2 production of BBS, BOB-OVs and BBS/BOB-2.

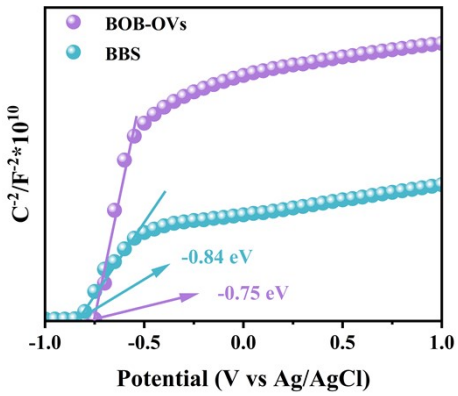

Figure S26. M-S curves of BOB-OVs and BBS.

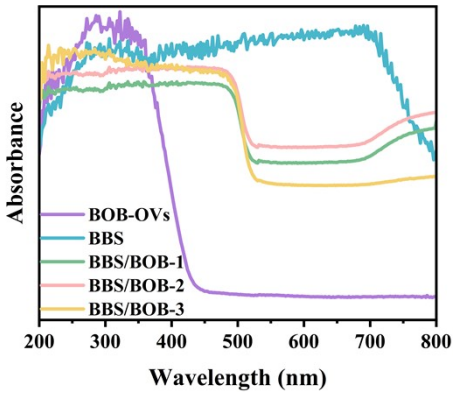

Figure S27. UV-Vis diffuse reflectance spectra of BOB-OVs, BBS, and BBS/BOB composite materials.

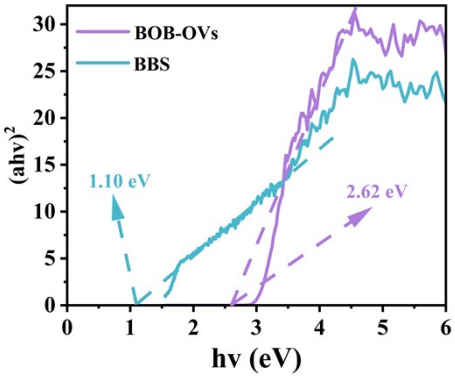

Figure S28. The plots of $(\alpha hv)^{1/2}$ versus photon energy (hv) for BOB-OVs and BBS.

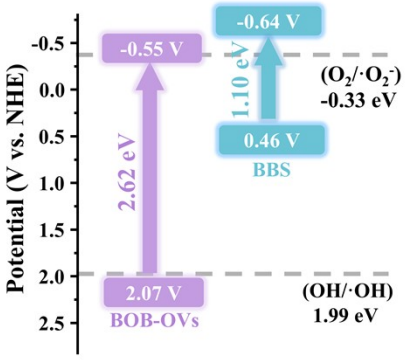

Figure S29. the band energy diagram of BOB-OVs and BBS.

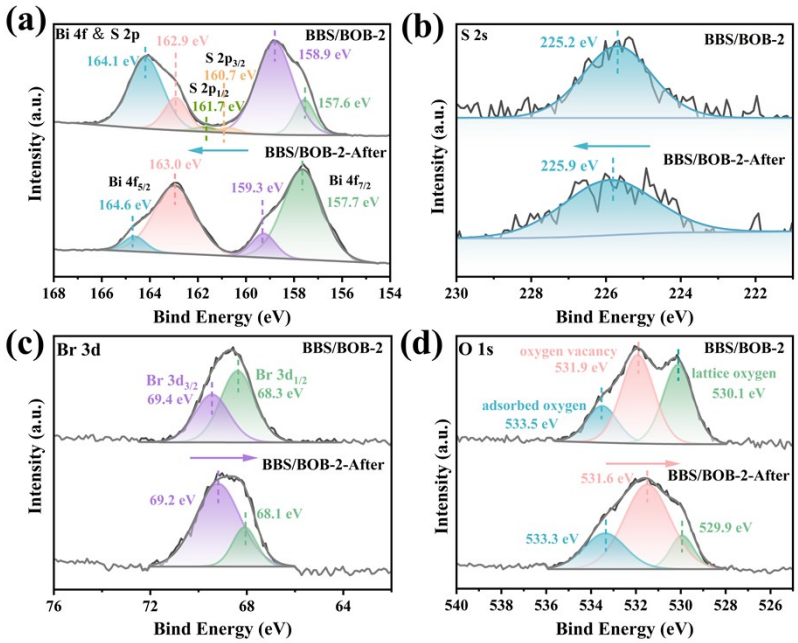

Figure S30. The high-resolution XPS spectra of (a) Bi 4f and S 2p, (b) S 2s, (c) Br 3d and (d) O 1s before and after photocatalytic OFX by BBS/BOB-2.

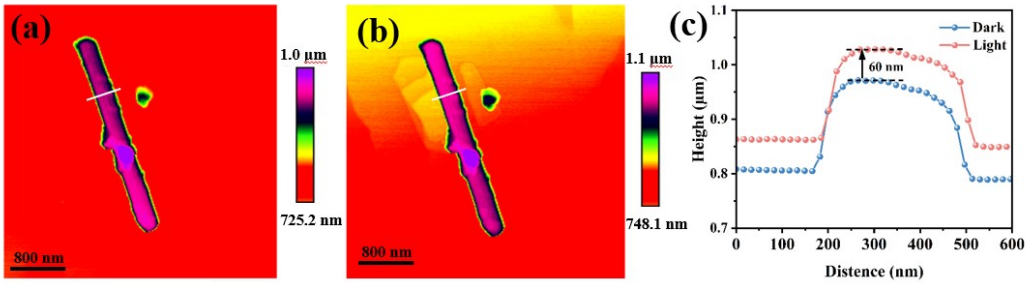

Figure S31. Surface morphology image of BBS/BOB-2 (a) under dark and (b) illuminated conditions. (c) The height profile image along white line.

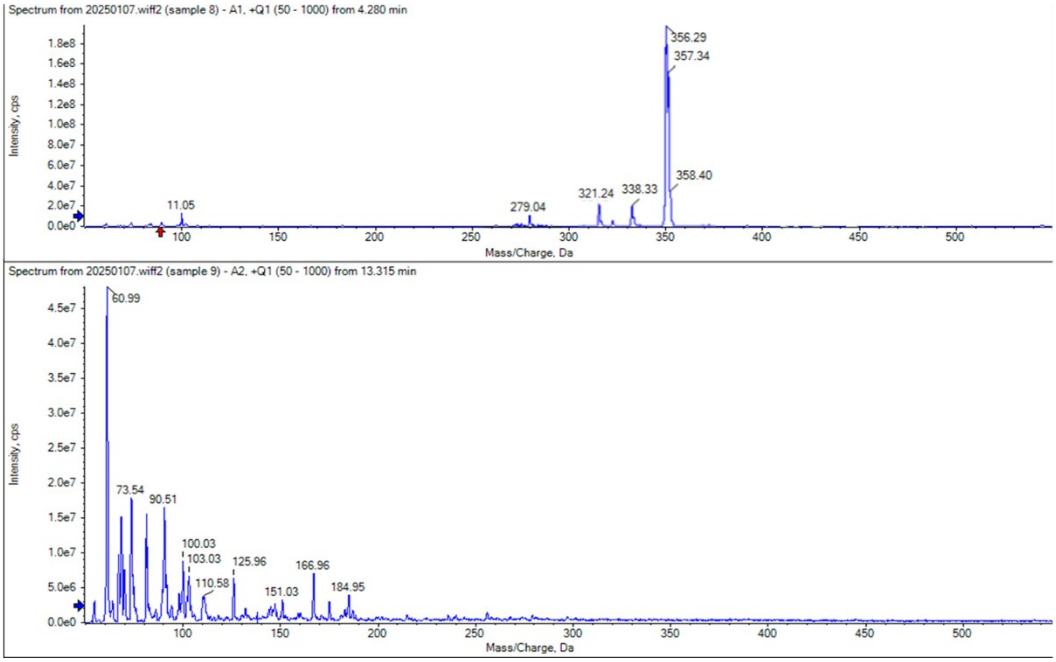

Figure S32. MS analysis.

Table S1. The parameter obtained from Nitrogen adsorption-desorption isotherm curves of BOB, BBS, BBS/BOB-1, BBS/BOB-2 and BBS/BOB-3

Samples	S_{BET}($m^2 \cdot g^{-1}$)	D_m(nm)
BOB	67.45	10.42
BBS	148.08	6.60
BBS/BOB-1	150.10	7.45
BBS/BOB-2	108.42	9.13
BBS/BOB-3	64.77	8.94

S_{BET} BET specific surface area; D_m average pore diameters

Table S2. kinetic parameters of samples

Photocatalysts	BOB	BBS	BBS/BOB-1	BBS/BOB-2	BBS/BOB-3
K(min^{-1})	0.0264	0.0732	0.1543	0.1971	0.1078
R^2	0.98	0.97	0.96	0.93	0.98

Table S3. Comparison of photocatalytic properties of OFX by different photocatalysts

Photocatalysts	experiment condition (Solid-liquid ratio, light intensity, pollutant concentration)	Degradation time	rate constant of pseudo-first-order kinetics	Removal rate	Ref
h-WO_3	0.2 g/L; 8 W mercury UV lamp; 35 mg/L	150 min	0.0156 min^{-1}	93.20 %	S2
Y_2O_3/BiOCl	0.5 g/L; 300 W xenon lamp; 20 mg/L	120 min	0.0151 min^{-1}	87.81 %	S3
MBiOBr-2CoPc	0.2 g/L; 300 W xenon lamp; 2 mg/L	20 min	0.165 min^{-1}	96.00 %	S4
$BiFeO_3$	0.5 g/L; 85 W CFL Bulb; 10 mg/L	180 min	0.0097 min^{-1}	80.00 %	S5
MCN-60	0.25 g/L; 300 W xenon lamp; 10 mg/L	150 min	0.0271 min^{-1}	96.50 %	S6
m-PDI	0.2 g/L; 300 W xenon lamp; 15 mg/L	60 min	0.07481 min^{-1}	~100%	S7
50-BIM	1.0 g/L; 500 W xenon lamp; 20 mg/L	14 min	0.022 min^{-1}	90.90 %	S8
TBN-8	0.1 g/L; 300 W xenon lamp; 20 mg/L	120 min	0.0475 min^{-1}	99.80 %	S9
BBS/BOB-2	0.4 g/L; 200 W xenon lamp; 10 mg/L	20 min	0.1971 min^{-1}	97.63 %	This work

Table S4. Obtained acute and chronic toxicity of OFX and its degradation products using T.E.S.T program.

Chemical	Daphnia magna LC50	Fathead minnow LC50	Mutagenicity	Development toxicity
OFX	34.56	2.74	0.58	0.93
P1	20.63	5.50	0.53	0.72
P2	250.89	62.07	0.90	0.51
P3	769.27	165.92	0.63	0.22
P4	7.05	3.26	0.71	1.07
P5	114.07	1347.07	0.08	0.74
P6	6.33	5.70	0.86	0.53
P7	25.40	287.63	0.23	0.66
P8	170.98	1305.91	0.24	0.51
P9	26.88	30.19	0.13	0.78
P10	253.64	303.68	0.11	0.68
P11	109.71	397.18	0.49	0.66

References

S1 F. Chen, K. Zhu, A. Chen, W. Huang, L. Feng, Z. Zhou,G. Ge, *Appl. Surf. Sci.*, 2013, **280**, 655-659.

S2 A. J. Antony, R. B. Bennie, C. Joel, N. Basavegowda, M. R. Hatshan,Y. A. Kumar, *J. Alloys Compd.*, 2025, **1019**, 179305.

S3 J. Luo, L. Wu, D. Liu, Y. Chen, Q. Lv,H. Deng, *J. Alloys Compd*, 2024, **1010**, 177888.

S4 R. Chen, W. Gan, J. Guo, J. Huang, S. Ding, R. Liu, Z. Zhao, K. Yan, Z. Zhou, M. Zhang,Z. Sun, *Sep. Purif. Technol.*, 2024, **360**, 131034.

S5 G. Gupta, S. K. Kansal, A. Umar,S. Akbar, *Chemosphere*, 2022, **314**, 137611.

S6 S. Qi, L. Jiang, Y. Huayu, W. Bin, W. Yuehu, L. Yancheng,X. Yi, *Chem. Eng. J.*, 2021, **427**, 131594.

S7 C. Huang, W. Yu, N. Fang, C. He, Y. Chu,B. Lai, *Sep. Purif. Technol.*, 2024, **360**, 131146.

S8 Y. Wang, L. Sun,H. Liu, *Chem. Eng. J.*, 2025, **507**, 160777.

S9 C. Yu, G. Hu, X. Zhang, C. Song, Y. Wang, J. Lin, Y. Zhang, Z. Liu, Z. Guo, C. Tang,Y. Huang, *J. Alloys Compd.*, 2023, **970**, 172548.